Surface structure modification of $ReSe_2$ nanosheets via carbon ion irradiation

Mei Qiao(乔梅)[1], Tie-Jun Wang(王铁军)[1,†], Yong Liu(刘泳)[2], Tao Liu(刘涛)[3], Shan Liu(刘珊)[1], and Shi-Cai Xu(许士才)[1,‡]

[1] *College of Physics and Electronic Information, Shandong Key Laboratory of Biophysics, Dezhou University, Dezhou* 253023, *China*
[2] *School of Physics, State Key Laboratory of Crystal Materials and Key Laboratory of Particle and Particle Irradiation (MOE), Shandong University, Jinan* 250100, *China*
[3] *School of Electronic and Information, Qingdao University, Qingdao* 266071, *China*

(Received 19 March 2022; revised manuscript received 8 May 2022; accepted manuscript online 24 May 2022)

The effects of C ion irradiation on multilayer $ReSe_2$ flakes are studied by utilizing different kinds of technologies. The domain sizes, thickness, morphologies of the multilayer $ReSe_2$ flakes on the Al_2O_3 substrates before and after 1.0-MeV C ion irradiation with different fluence rates are studied by atomic force microscope and scanning electron microscopy. The atomic vibrational spectra of multilayer $ReSe_2$ flakes are detected by micro-Raman spectra. The redshifts of the Raman modes after 1.0-MeV C ion irradiation are observed from the micro-Raman spectra. The elemental compositions and bonding configurations of the multilayer $ReSe_2$ samples before and after irradiation processes are characterized by x-ray photoelectron spectroscopy. The structural properties are also investigated by x-ray diffraction, and it is concluded that after 1.0-MeV C ion irradiation process, multilayer $ReSe_2$ samples continue to grow on Al_2O_3 substrates, the increase of crystallite size also reveals that the crystallinity is improved with the increase of the layer number after 1.0-MeV C ion irradiation.

Keywords: ion irradiation, microstructure, crystallinity, surface morphology

PACS: 61.05.–a, 61.05.cp, 61.46.–w, 61.72.–y **DOI:** 10.1088/1674-1056/ac7297

1. Introduction

Owing to the unique optical and electronic properties, transition metal dichalcogenides (TMDs) have been widely studied, showing that TMD has a great potential application in beyond-CMOS devices.[1–8] Among the TMDs, $ReSe_2$ crystallizes belong to the triclinic system, and the cluster of Re_4 units forms a one-dimensional (1D) chain inside each monolayer, with layers held together by van der Waals attraction.[9] Generally, most VI TMDs such as MoS_2 and WS_2 show more superior performances due to their monolayer structure, while unlike other two-dimensional (2D) materials, $ReSe_2$ shows very weak layer-dependent optical and vibrational properties.[10,11] The stabilization of the extra valence electron in each Re atom can result in inherent lattice distortion in $ReSe_2$, which makes it a suitable candidate for tuning the optical properties via strain engineering.[12] The multilayer $ReSe_2$ flakes have been demonstrated as field-effect transistors (FETs), digital inverters, and photodetectors.[13,14] However, the synthesis technology of $ReSe_2$ nanosheet is more complicated than those of other TMDs such as MoS_2 and WS_2, due to its properties (like structure, crystal quality, domain size, thickness, and morphology) are difficult to modify accurately.[15,16] Unlike hexagonal layered TMDs such as MoS_2 and WS_2, the $ReSe_2$ with anisotropy shows the potential in fabricating versatile devices, and it is essential to develop modification strategy to improve properties of $ReSe_2$ for practical applications.[12] In recent years, a large amount of work on ion beam modification of 2D or other film materials has been performed, showing an effective way to modify $ReSe_2$.[17–24]

In this work, the properties of multilayer $ReSe_2$ samples on Al_2O_3 substrates are modified by ion irradiation technique. The irradiated C ions lose energy through two mechanisms: nuclear energy loss (originating from nucleus collision) and electronic energy loss (arising from interaction between irradiated electron and lattice atoms). The micro-structure and related properties of multilayer $ReSe_2$ sample are modified through these two energy-losing mechanisms. The surface morphologies, including the size, thickness, microstructure, elemental analysis, bonding configurations, and crystallinity of the multilayer $ReSe_2$ samples, are studied after 1.0-MeV C ion irradiation at fluence rates of 5.0×10^{13} ions/cm^2 and 5.0×10^{14} ions/cm^2. The results indicate that the domain sizes, thickness, crystallinities, and morphologies of the $ReSe_2$ samples can be effectively controlled by ion irradiation process.

2. Materials and methods

The multilayer $ReSe_2$ samples were grown on the single crystal Al_2O_3 by the CVD with dimensions of 5.0 mm×5.0 mm×0.5 mm, and irradiated by 1.0-MeV C ions

†Corresponding author. E-mail: Wtj.sdu@foxmail.com
‡Corresponding author. E-mail: shicaixu@dzu.edu.cn

© 2023 Chinese Physical Society and IOP Publishing Ltd

at the fluences of 5.0×10^{13} ions/cm^2 and 5.0×10^{14} ions/cm^2 from a 2×1.7-MV tandem accelerator[25] at room temperature ($\sim$ 300 K). The details of the ions irradiated on multilayer $ReSe_2$ flakes on crystalline Al_2O_3 are displayed in Table 1.

Table 1. Details of ion irradiated multilayer $ReSe_2$ flakes on crystalline Al_2O_3.

Sample	Irradiated ion	Energy (MeV)	Fluence rate (ions/cm^2)
S0	–	–	–
S1	C	1.0	5.0×10^{13}
S2	C	1.0	5.0×10^{14}

The ion irradiation effects in multilayer $ReSe_2$ samples were characterized by utilizing atomic force microscope (AFM), scanning electron microscopy (SEM), micro-Raman spectra, x-ray photoelectron spectroscopy (XPS), and x-ray diffraction (XRD). The thickness of non-irradiated and irradiated $ReSe_2$ flakes were characterized by AFM on NT-MDT model BL222 RNTE. The peak force amplitude and scan rate were 150 nm and 0.977 Hz, respectively. Surface morphologies, including the sizes and shapes of the multilayer $ReSe_2$ samples, were determined by SEM imaging on a Hitachi S-4800. The imaging resolution and accelerating voltage were 1.0 nm and 5 kV, respectively. The detailed Raman peak positions and a comparison before and after ion irradiation were obtained at room temperature by using a multichannel modular triple Raman system (HORIBA Jobin-Yvon HR800) at 632.8-nm excitation wavelengths. The spot diameters of the focused laser beam on the multilayer $ReSe_2$ samples were all about 1.0 μm. The core level elemental analysis and bonding configurations of the multilayer $ReSe_2$ samples were performed by XPS on an ESCALAB 250. Monochromatic Al K_α x-ray source (1486.6 eV) and hemispherical deflector analyser were used in the XPS spectrometer, working at constant pass energy, and constant energy resolution on the whole spectrum can be maintained with this mode. Intrinsic resolution of the spectrometer was 0.45 eV, which was proved by the the Ag $3d_{5/2}$ line. The x-ray spot in this experiment was about 150-μm diameter. The XRD experiments were conducted to structurally analyze the samples with Cu $K\alpha$ emission ($\lambda = 1.54056$ Å) on a Rigaku RINT-2500 VHF x-ray diffractometer. The diffraction patterns were recorded between 10° and 30° on a 2θ scale in steps of 0.04°.

3. Results and discussion

In Fig. 1, AFM images of multilayer $ReSe_2$ surface non-irradiated and irradiated with 1.0-MeV C ions at fluence of 5.0×10^{13} ions/cm^2 and 5.0×10^{14} ions/cm^2 are shown. The typical shape and corresponding height profile of multilayer $ReSe_2$ are determined by AFM and the reults are displayed in Figs. 1(a)–1(f). The $ReSe_2$ flakes on Al_2O_3 substrates display quadrilateral shape before irradiation and then turn into oval shapes after being processed. The change of shape can be attributed to the difference in edge formation energy between the Re edge and Se edge termination before and after being irradiated by C ions . After the irradiation of 1.0-MeV C ions, the specific edge termination effect was destroyed, and oval shapes form in the multilayer $ReSe_2$. Thickness of the monolayer $ReSe_2$ flake is approximately in a range of 0.7 nm–0.8 nm.[9] In Fig. 1, the observed thickness values of the $ReSe_2$ samples are approximately 2.8, 6.4, and 9.1 nm corresponding to flakes consisting of 4, 9, and 13 layers for samples S0, S1, and S2, respectively. Through the collision cascade, the atoms of $ReSe_2$ acquire higher energy than that due to the van der Waals' forces. Then, the $ReSe_2$ flakes continue to grow and the thickness values of the $ReSe_2$ flakes increase after the irradiation of 1.0-MeV C ions.

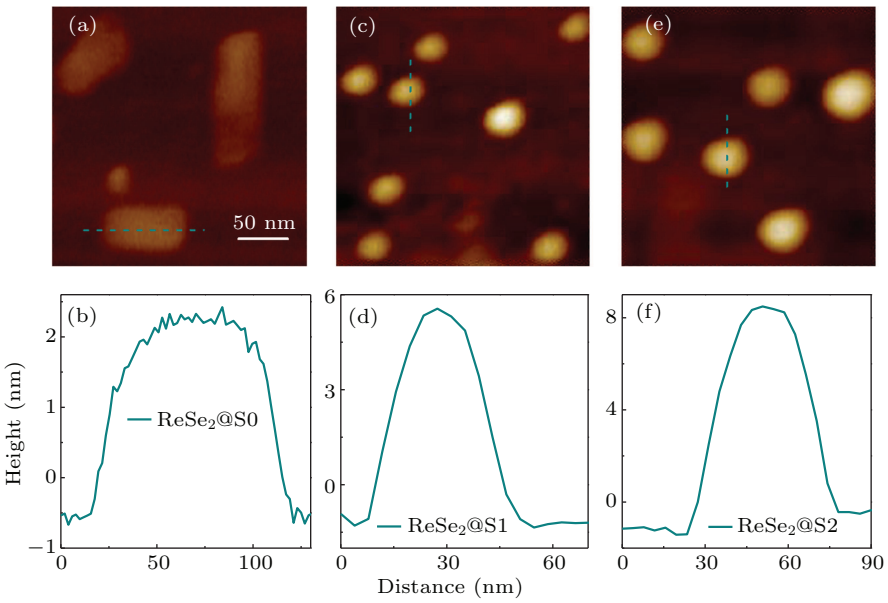


Fig. 1. AFM images for multilayer $ReSe_2$: (a) 2D image and (b) height profile for sample S0; (c) 2D image and (d) height profile for sample S1; (e) 2D image and (f) height profile for sample S2.

The surface morphologies before and after 1.0-MeV C ions irradiation are determined by using SEM technique and shown in Fig. 2. Figure 2(a) shows that the surface profile of the non-irradiated multilayer $ReSe_2$ is relatively smooth and uniform. Figure 2(b) displays a magnified view of the non-irradiated multilayer $ReSe_2$. After the irradiation of 1.0-MeV C ions, the morphologies of the samples S1 and S2 are greatly changed. After the irradiation of 1.0-MeV C ions at the fluence rate of 5.0×10^{13} ions/cm^2, pores with diameters in a range of 10 μm–25 μm are evenly located on the multilayer $ReSe_2$ sample (as shown in Fig. 2(c)). Figure 2(d) shows that the particles of $ReSe_2$ are perfectly oval with a uniform size distribution. The long diameter and short diameter of the $ReSe_2$ nanoparticles (sample S2) are approximately 3.0 μm and 1.0 μm, respectively. The average distance between the nanoparticles is approximately 17.0 μm. A higher irradiation fluence causes great damaging effects on the dimensions of the samples. It is an effective way to modify sample size by controlling the irradiation conditions.

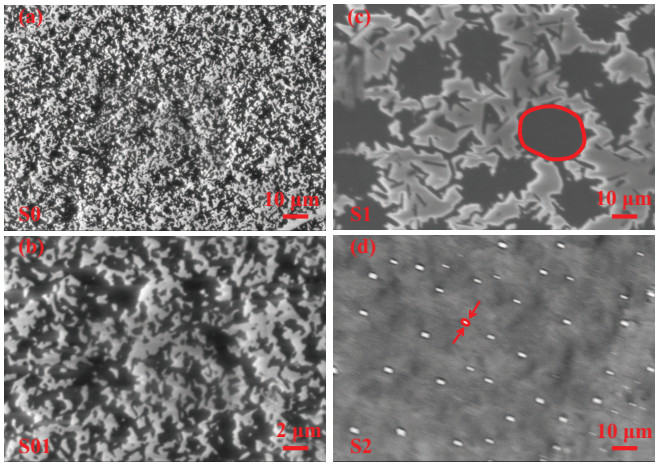


Fig. 2. SEM images of multilayer $ReSe_2$ samples under different irradiation conditions: (a) sample S0 (unirradiated), (b) high-magnification for sample S0, (c) sample S1 (1.0-MeV C ions at a fluence of 5.0×10^{13} ions/cm^2), and (d) sample S2 (1.0-MeV C ions at a fluence of 5.0×10^{14} ions/cm^2).

The atomic vibrational spectra of multilayer $ReSe_2$ flakes after the irradiation of 1.0-MeV C ions at the fluence rates of 5.0×10^{13} ions/cm^2 and 5.0×10^{14} ions/cm^2 are detected in a range of 100 cm^{-1}–300 cm^{-1} and are shown in Fig. 3. Unlike the Raman spectra of MoX_2 and WX_2 (X = S, Se), the Raman spectra of the $ReSe_2$ are feature-rich with approximately 18 first-order Raman-active modes in the range of 100 cm^{-1}–300 cm^{-1}, which are nondegenerate due to their low-symmetry triclinic structure.[9] For $ReSe_2$, it is difficult to determine a pure vibration mode because of the complicated crystal lattice. Therefore, we name the Raman modes based on the dominant direction of the phonon vibrations. As shown in Fig. 3, the Raman peaks at 121 cm^{-1} results from the in-plane vibrational mode (E_g-like) and at 163 cm^{-1} and 176 cm^{-1} originate from the out-of-plane vibrational mode (A_g-like).[26]

The thickness values of $ReSe_2$ layers after being irradiated by 1.0-MeV C ions are measured from the AFM images and shown in Fig. 1. With the increase of sample thickness, most of the peaks for the few-layer $ReSe_2$ are red-shifted (Fig. 3). Only considering the long-range Coulombic interactions, the Coulombic screening can be increased by the increasing dielectric tensors that augment with the number of layers increasing. This results in a softer Coulombic interaction between atoms, and therefore, the redshift takes place in the corresponding Raman peaks.[27] However, if we consider the van der Waals force, the interaction between the layers tends to suppress the lattice vibrations with the number of layers increasing. Thus, the vibrational energy of each vibration mode can increase, thereby leading to blueshift.[28] We know that the atomic mass of $ReSe_2$ is almost equal to that of WSe_2. For WSe_2, the E_{2g} and A_{1g} modes show the changes of redshift and blueshift from the monolayer to the bulk, respectively.[29] The strength of Coulombic screening can be measured by the ratio of the long-range coulomb interaction of the monolayer to that of the bulk,

$$\begin{aligned} & C^{\mathrm{lr}}_{M,xM,x}(\mathrm{mono})/C^{\mathrm{lr}}_{M,xM,x}(\mathrm{bulk}) \\ = \; & (Z^{*}_{M,xx,\mathrm{mono}}/Z^{*}_{M,xx,\mathrm{bulk}})^2 \\ & \times\sqrt{\varepsilon_{xx,\mathrm{bulk}}\varepsilon_{zz,\mathrm{bulk}}/\varepsilon_{xx,\mathrm{mono}}\varepsilon_{zz,\mathrm{mono}}}. \end{aligned} \tag{1}$$

The details can be found in previous work.[26] From the above equation, we can determine that the long-range Coulombic interactions in WSe_2 and $ReSe_2$ are similar to each other. In addition, the interlayer force constant $\alpha \propto \mu\omega$ can be used to measure the van der Waals interaction, where m and w are the atomic mass of the monolayer TMDCs and the Raman frequency, respectively. From Ref. [30], the frequency of the C mode and the LB mode in bilayer WSe_2 are higher than those in bilayer $ReSe_2$. The calculations show that the interlayer van der Waals interaction of $ReSe_2$ is much weaker than that of WSe_2. According to the above discussion, with the number of $ReSe_2$ layers increasing, the redshifts of the Raman modes after the irradiation of 1.0-MeV C ions as shown in Fig. 3 indicate that the interlayer van der Waals interaction is not strong enough to determine the layer dependence of the phonon behavior.

However, the Raman mode at 163 cm^{-1} mainly involves the atomic displacement of the Re–Re bond.[31] After the irradiation of 1.0-MeV C ions, the Raman mode is located at 162.5 cm^{-1} for sample S1 and at 161.7 cm^{-1} for sample S2. Under the above condition, we can determine that a longer bond length for the Re–Re bond occurs due to the volume expansion induced by irradiation, with the $ReSe_2$ layer number increasing.

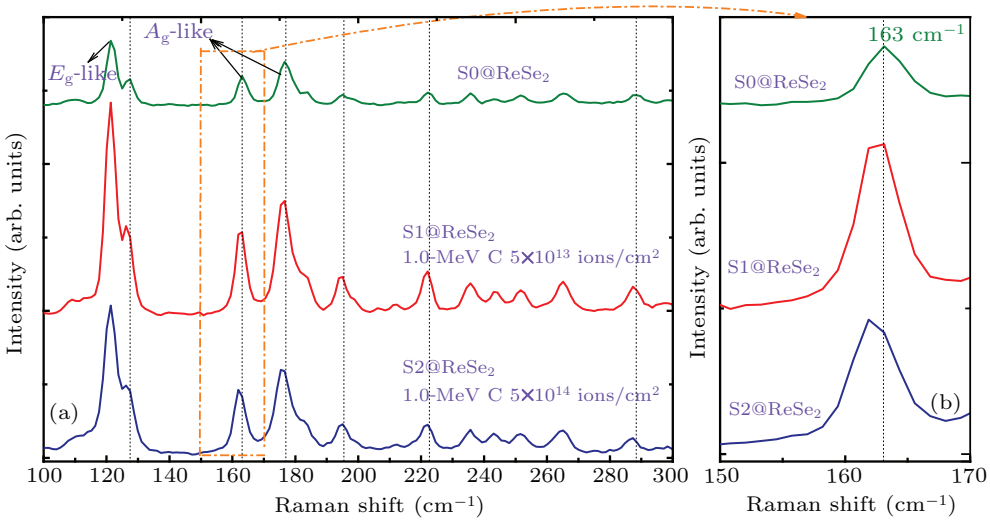


Fig. 3. Raman spectra obtained at 632.8-nm excitation energy for multilayer $ReSe_2$ flakes irradiated under different conditions.

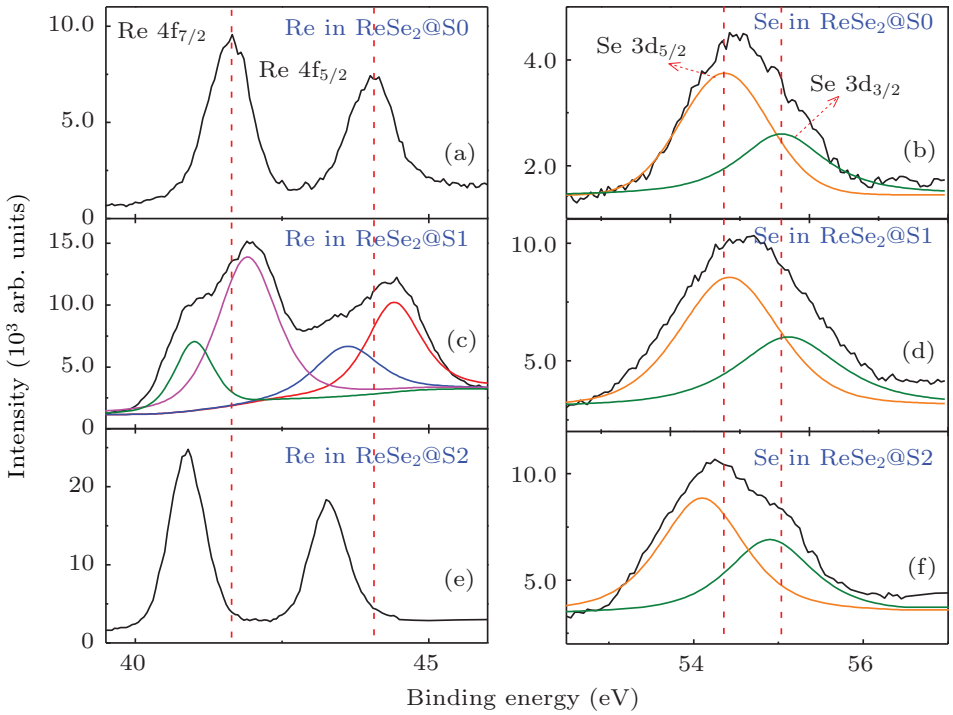


Fig. 4. XPS spectra of multilayer $ReSe_2$ flakes before and after the irradiations of 1.0-MeV C ions.

The elemental compositions and bonding configurations of the multilayer $ReSe_2$ samples are characterized by XPS. The detailed information regarding the Re signal and Se signal is exhibited in Figs. 4(a), 4(c), 4(e) 4(b), 4(d), and 4(f), respectively. As shown in Fig. 4(a), two characteristic peaks located at 41.6 eV and 44.1 eV are observed, which correspond to the core $4f_{7/2}$ and $4f_{5/2}$ levels of Re^{4+}. Additionally, figure 4(b) shows clearly resolved Se^{2-} $3d_{5/2}$ and $3d_{3/2}$ peaks at 54.78 eV and 55.61 eV determined via the curve fitting. The two characteristic peaks are consistent with the results reported in Ref. [32], and the curve fitting method is based on the XPS peak code. Additionally, the ratio of Re to Se acquired from XPS is nearly 1:2, which suggests that the CVD-grown $ReSe_2$ is reasonably stoichiometric.

To further analyze the change of multilayer $ReSe_2$ after the irradiation of 1.0-MeV C ions , the shift of XPS peak is studied and shown in Figs. 4(c)–4(f). The peak position shift of XPS is a combined result of three main factors. First of all, the defects induced by ion irradiation will result in surface energy band bending and the peak value shifts to a higher energy value. Meanwhile, the irradiation-induced defects and lattice-disorder will also lead the lattice volume to expand, and further cause longer bond length of the Re–Re bond, with irradiated fluence increasing. The longer Re–Re bond length is apparently corresponding to weaker bond strength, which causes the binding energy to shift to a lower energy value. Furthermore, C ion irradiation will induce partial electron to transfer, and part of Re^{4+} ions are converted into Re^{2+} ions, which leads

the binding energy to decrease.

The XPS result of Re 4f in Fig. 1(c) shows two spin–orbit split peaks with a separation of 2.5 eV, which correspond to $4f_{7/2}$ and $4f_{5/2}$ respectively. Apparently, the Re $4f_{7/2}$ peak can be fitted by two peaks, *i.e.*, the dominant peak at 41.9 eV (the characteristics of n-type doping), which is due to the surface energy band bending effect induced by defect, and the weaker peak at 41.0 eV, which is attributed to the volume expansion of lattice and the presence of Re^{2+} ion. The Re $4f_{5/2}$ peak can also be fitted by two peaks, out of the same reason. In addition, as shown in Fig. 4(e), the Re $4f_{7/2}$ peak value of sample S2 shifts by 0.7 eV, reasching a lower energy value, which shows that lattice volume expansion and the role of Re^{2+} ion are dominated in sample S2. As a conclusion, the shift of XPS peak shows an oscillatory trend with fluence increasing, which is determined by the joint action of irradiation induced defects, lattice-expansion effect and the role of Re^{2+} ion.

The XRD is used to evaluate the structural characteristics of multilayer $ReSe_2$ flakes under the different irradiation conditions, and the results are shown in Fig. 5. For samples S0, S1, and S2, most of significant (001) peaks are observed at $2\theta = 13.00°$, 13.76°, and 13.65°, respectively. The XRD pattern is consistent with the JCPDS card No. 89-0340, wihch indicates the presence of the triclinic phase for multilayer $ReSe_2$. The interplanar spacings are approximately 6.8712 Å, 6.4306 Å, and 6.4811 Å from Jade 6.0 for samples S0–S2, respectively. Nonirradiated $ReSe_2$ flakes (S0) yield a very noisy powder XRD pattern with lines of weak intensity and wide FWHM, indicating poor crystallinity of the sample S0. After the irradiation of 1.0-MeV C ions, which causes the $ReSe_2$ to grow, the thickness of the $ReSe_2$ layer increases, the intensity of the diffraction peak strengthens, and the FWHM decreases. This indicates that the crystallinity of the $ReSe_2$ flake is improved with the number of layers increasing after the irradiation of 1.0-MeV C ions . Comparing with non-irradiated $ReSe_2$ flakes (sample S0), the intensity of the diffraction peak is improved by approximately 148% for sample S1 and 180% for sample S2. In addition, the FWHM values of the (001) diffraction peakare approximately 2.15°, 0.92°, and 0.87°, for samples S0, S1, and S2 respectively. From the above data, the average crystallite size can be calculated using the Debye–Scherer equation

$$D = \lambda/(\beta\cos\theta). \tag{2}$$

The details can be found in Ref. [33]. From Eq. (2), we can determine the average crystallite size $D_0 = 3.67$ nm (sample S0), $D_1 = 8.65$ nm (sample S1), and $D_2 = 9.09$ nm (sample S2). The increased crystallite size can also reveal that the crystallinity is improved with the increase of the number of layers after the irradiation of ions. As a result, comparing with the data of samples detected by XRD, AFM, and SEM, it is apparent that samples S1 and S2 show almost the same crystalline quality and grain size, which means that the irradiated condition of S1 (with lower fluence means cost-effective and lower irradiation effect) is more appropriate for $ReSe_2$ samples.

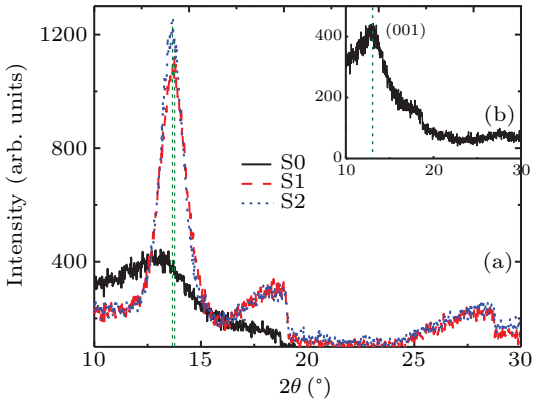


Fig. 5. XRD patterns (θ–2θ) of multilayer $ReSe_2$ flakes before and after being irradiated by 1.0-MeV C ions.

4. Conclusions

In this work, the effect of C ion irradiation of multilayer $ReSe_2$ flakes has been studied and characterized by utilizing AFM, SEM, micro-Raman spectra, XPS, and XRD. The results confirm that that the domain size, thickness, morphology, and crystallinity for the $ReSe_2$ sample can be effectively controlled after the irradiation of 1.0-MeV C ions. Through appropriately regulating the energy and fluence of C ions , multilayer $ReSe_2$ samples with high-quality crystallinity, relatively large size and good performance can be obtained.

Acknowledgements

Project supported by the National Natural Science Foundation of China (Grant Nos. 12105036, 11775135, and 11805108), the Natural Science Foundation of Shandong Province, China (Grant Nos. ZR2020QA088 and ZR2021QA074), the Taishan Scholars Program of Shandong Province, China (Grant No. tsqn201812104), and the State Key Laboratory of Nuclear Physics and Technology at Peking University, China.

References

[1] Apte A, Krishnamoorthy A, Hachtel J A, Susarla S, Yoon J, Sassi L M, Bharadwaj P, Tour J M, Idrobo J C, Kalia R K, Nakano A, Vashishta P, Tiwary C S and Ajayan P M 2019 *Nano Lett.* **19** 6338
[2] Simchi H 2019 *Chin. Phys. B* **29** 027401
[3] Li Y, Fu R Z, Duan Z G, Zhu C H and Fan D D 2022 *Bioact. Mater.* **9** 461
[4] Zhang Q, Ying H, Li X, Xiang R, Zheng Y, Wang H, Su J, Xu M, Zheng X, Maruyama S and Zhang X 2021 *ACS Appl. Mater. Inter.* **13** 31861
[5] Wu Y K, Zhong W, Yang Q J, Hao C, Li Q L, Xu M O and Bao S J 2021 *Chem. Eng. J.* **427** 130960
[6] Li X M, Deng J X, Liu L L, Zhang L L, Sun J, Ge D L, Liu Y Y and Duan R 2018 *Surf. Coat. Tech.* **352** 128

[7] Bian C, Shi J, Liu X, Yang Y, Yang H and Gao H 2022 *Chin. Phys. B* **31** 097304

[8] Ernandes C, Khalil L, Almabrouk H, Pierucci D and Ouerghi 2021 *npj 2D Mater. Appl.* **5** 7

[9] Wolverson D, Crampin S, Kazemi A S, llie A and Bending A J 2014 *ACS Nano* **8** 11154

[10] Jariwala B, Voiry D, Jindal A, Chalke B A, Bapat R, Thamizhavel A, Chhowalla M, Deshmukh M and Bhattacharya A 2016 *Chem. Mater.* **28** 3352

[11] Tongay S, Sahin H, Ko C, Luce A, Fan W, Liu K, Zhou J, Huang Y S, Ho C H, Yan J, Ogletree D F, Aloni S, Ji J, Li S, Li J, Peeters F M and Wu J 2014 *Nat. Commun.* **5** 3252

[12] Yang S, Wang C, Sahin H, Chen H, Li Y, Li S S, Suslu A, Peeters F M, Liu Q, Li J and Tongay S 2015 *Nano Lett.* **15** 1660

[13] Yang S, Tongay S, Yue Q, Li Y, Li B and Lu F 2014 *Sci. Rep.* **4** 5442

[14] Wang X, Huang L, Peng Y, Huo N, Wu K, Xia C, Wei Z, Tongay S and Li J 2016 *Nano Res.* **9** 507

[15] Cui F, Li X, Feng Q, Yin J, Zhou L, Liu D, Liu K, He X, Liang X, Liu S, Lei Z, Liu Z, Peng H, Zhang J, Kong J and Xu H 2017 *Nano Res.* **10** 2732

[16] Xie C, Jiang S, Zou X, Sun Y, Zhao L, Hong M, Chen S, Huan Y, Shi J and Zhou X 2019 *Nano Res.* **12** 149

[17] Naitou Y and Ogawa S 2016 *Appl. Phys. Lett.* **108** 171605

[18] Fujiwara H, Norizuki R, Miura S, Kano S, Tanaka T, Inami W, Kawata Y and Chikada T 2022 *Nucl. Mater. Energy* **30** 101141

[19] Pantousa S, Mergia K, Ionescu A, Manios E, Dellis S, Kinane C, Langridge S, Caruana A, Kentsch U and Messoloras S 2022 *Nucl. Mater. Energy* **30** 101147

[20] Song H L, Yu X F, Chen M, Qiao Mei, Wang T J, Zhang J, Liu Y, Liu P and Wang X L 2018 *Appl. Surf. Sci.* **439** 240

[21] Luxa J, Mazánek V, Mackova A, Malinsky P, Akhmadaliev S and Sofer Z 2018 *Appl. Mater. Today* **14** 216

[22] Zhang N, Liu B and Lin L W 2020 *Acta Phys. Sin.* **69** 016101 (in Chinese)

[23] Jiang M Y, Zhu Z J, Chen C K, Li X and Hu X J 2019 *Acta Phys. Sin.* **68** 148101 (in Chinese)

[24] Wang J L, Chen C K, Li X, Jiang M Y and Hu X J 2020 *Chin. Phys. B* **29** 018103

[25] Liu P 2013 *Waveguide formation, scintillation response and damage properties of functional crystal materials under MeV ion irradiation* Ph.D. dissertation (Jinan: Shandong university) (in Chinese)

[26] Hafeez M, Gan L, Li H, Ma Y and Zhai T 2016 *Adv. Mater.* **28** 8296

[27] Molina-Sánchez A and Wirtz L 2011 *Phys. Rev. B* **84** 155413

[28] Zhang X, Qiao X F, Shi W, Wu J B, Jiang D S and Tan P H 2015 *Chem. Soc. Rev.* **44** 2757

[29] Zhao W, Ghorannevis Z, Kumar A K, Pang J R, Toh M, Zhang X, Kloc C, Tan P H and Eda G 2013 *Nanoscale* **5** 9677

[30] Zhao H, Wu J, Zhong H, Guo Q, Wang X, Xia F, Yang L, Tan P and Wang H 2015 *Nano Res.* **8** 3651

[31] Feng Y, Zhou W, Wang Y, Zhou J, Liu E, Fu Y, Ni Z, Wu X, Yuan H, Miao F, Wang B, Wan X and Xing D 2015 *Phys. Rev. B* **92** 054110

[32] Qi F, Wang X, Zheng B, Chen Y, Yu B, Zhou J, He J, Li P, Zhang W and Li Y 2017 *Electrochim. Acta* **224** 593

[33] Jiang C H 2014 *The technique and application of polycrystalline x-ray diffraction*, (Vol. 1) (Beijing: Chemical Industry Press) pp. 62–63 (in Chinese)